# Coherent structures, intermittent turbulence, and dissipation in high-temperature plasmas

H. Karimabadi, V. Roytershteyn, M. Wan, W. H. Matthaeus, W. Daughton et al.

Citation: Phys. Plasmas **20**, 012303 (2013); doi: 10.1063/1.4773205
View online: http://dx.doi.org/10.1063/1.4773205
View Table of Contents: http://pop.aip.org/resource/1/PHPAEN/v20/i1
Published by the American Institute of Physics.

# Coherent structures, intermittent turbulence, and dissipation in high-temperature plasmas

H. Karimabadi,[1] V. Roytershteyn,[1] M. Wan,[2] W. H. Matthaeus,[2] W. Daughton,[3] P. Wu,[2] M. Shay,[2] B. Loring,[4] J. Borovsky,[5] E. Leonardis,[6] S. C. Chapman,[6,a)] and T. K. M. Nakamura[3]

[1]*Department of Electrical and Computer Engineering, University of California, San Diego, La Jolla, California 92093, USA*
[2]*University of Delaware, Department of Physics and Astronomy, Newark, Delaware 19716, USA*
[3]*Los Alamos National Laboratory, Los Alamos, New Mexico 87545, USA*
[4]*Lawrence Berkeley National Laboratory, Berkeley, California 94720, USA*
[5]*Space Science Institute, Boulder, Colorado 80301, USA*
[6]*Centre for Fusion, Space and Astrophysics, University of Warwick, Coventry, CV4 7AL, United Kingdom*

(Received 20 September 2012; accepted 7 December 2012; published online 16 January 2013)

An unsolved problem in plasma turbulence is how energy is dissipated at small scales. Particle collisions are too infrequent in hot plasmas to provide the necessary dissipation. Simulations either treat the fluid scales and impose an *ad hoc* form of dissipation (e.g., resistivity) or consider dissipation arising from resonant damping of small amplitude disturbances where damping rates are found to be comparable to that predicted from linear theory. Here, we report kinetic simulations that span the macroscopic fluid scales down to the motion of electrons. We find that turbulent cascade leads to generation of coherent structures in the form of current sheets that steepen to electron scales, triggering strong localized heating of the plasma. The dominant heating mechanism is due to parallel electric fields associated with the current sheets, leading to anisotropic electron and ion distributions which can be measured with NASA's upcoming Magnetospheric Multiscale mission. The motion of coherent structures also generates waves that are emitted into the ambient plasma in form of highly oblique compressional and shear Alfven modes. In 3D, modes propagating at other angles can also be generated. This indicates that intermittent plasma turbulence will in general consist of both coherent structures and waves. However, the current sheet heating is found to be locally several orders of magnitude more efficient than wave damping and is sufficient to explain the observed heating rates in the solar wind. © *2013 American Institute of Physics*. [http://dx.doi.org/10.1063/1.4773205]

## I. INTRODUCTION

Turbulence plays an important role in space and astrophysical plasmas by transferring energy through a cascading process from large scales to small scales, at which the turbulence can be dissipated. Examples of environments where turbulence is thought to play a significant role include heating of the solar corona and solar wind, and acceleration and transport of solar and galactic cosmic rays—all effects that establish the electrodynamic and radiation environment of the Earth. While large scale motions are well described by fluid theory,[1–5] the interface between fluid motions and kinetic plasma dynamics, and the identification of the dissipation process, remains an unsolved mystery.[6,7]

The multi-scale nature of turbulence that spans from MHD down to electron kinetic scales poses a severe computational challenge. As a result, simulations have either treated the fluid scales with an imposed *ad hoc* form of dissipation (e.g., resistivity)[4,8,9] or have been limited to kinetic scales with dissipation arising from resonant damping of small amplitude disturbances (e.g., Refs. 10 and 11). The fluid scale simulations show formation of current sheets that in turn provide the dominant dissipation mechanism. Electron kinetic scales are not resolved in such simulations. Simulations in this category include MHD,[5,8] Hall MHD,[4] particle-in-cell (PIC) hybrid (electron fluid, kinetic ions),[9,12] and Vlasov hybrid.[13] These studies show the tendency of the energy to accumulate in the perpendicular direction in the form of coherent structures. The Vlasov hybrid study[13] also shows the development of non-Maxwellian features in the ion distribution function concentrated in the proximity of regions with strong magnetic activity.

Alternatively, a second category of studies considers dissipation in the presence of a spectrum of small amplitude waves. The dissipation mechanism is found to result from the collisionless damping of the particular waves (e.g., whistlers, kinetic Alfven waves (KAW), and ion cyclotron waves) that are used for seeding and/or driving the initial perturbations in their simulations.[10,11] The type of waves that can be generated in such simulations is usually restricted. For example, gyrokinetic simulations do not contain proton or electron gyro-resonance effects, and whistler simulations have been too small to admit KAW. Boldyrev and Perez,[14] using a recently developed fluid model of KAW turbulence below the dispersion scale, have argued that the dissipative effects

[a)]Also at Department of Mathematics and Statistics, University of Tromso, Tomso, Norway.

 

may be less important at the subproton scales than was previously thought based on Landau damping arguments. While Rudakov *et al.*[15,16] using weak turbulence theory of KAW have emphasized the significant modification of the linear Landau damping effects of KAW due to quasi-linear evolution of the system away from a Maxwellian, effects that are not typically included in the gyrokinetic codes.[17] These reduced descriptions are valuable for studies of specific processes, but are not general descriptions of plasma physics at kinetic scales.

Motivated by these issues, we consider the development of turbulence from a laminar state in a shear driven cascade using fully kinetic two-dimensional (2D) and three-dimensional (3D) simulations that span the scales from MHD down to electron Debye length.[18] Fully kinetic particle codes are ideally suited for studies of turbulence and the associated dissipation since they include full kinetic effects of both electrons and ions but they are also the most computationally intensive. This first-principle study is made possible by the recent development of kinetic PIC code VPIC[19] that runs efficiently on full-scale modern supercomputers.

The reason for the focus on shear driven turbulence is twofold. First, shear flow is a canonical problem that serves as the building block in studies of turbulence,[6] dynamo,[20] and magnetorotational instability,[21] among others. Second, this focus will facilitate comparisons of our conclusions with copious kinetic scale observations being accumulated by spacecraft in solar wind in the vicinity of Earth orbit.[22–24] It is widely believed that turbulence in the solar wind is driven by velocity shears of varying sizes and strengths at both low and high latitudes.[25–29]

Through these simulations, we find that turbulent cascade leads to generation of coherent structures in the form of current sheets that steepen to electron scales, triggering strong localized heating of the plasma. The dominant heating mechanism is found to be due to parallel electric fields associated with the current sheets, leading to anisotropic electron and ion distributions. The current sheet heating is locally several orders of magnitude more efficient than wave damping, and is consistent with quantitative estimates of the observed heating rates in the solar wind. The motion of coherent structures generates waves that are emitted into the ambient plasma, analogous to the sound wave generation due to turbulent fluid motion in aeroacoustics.[30] This wave mechanism has not been considered in the solar wind and may lead to generation of waves that may otherwise not be possible. The implications of these results for theories of turbulence in general and heating of the solar wind in particular are discussed.

## II. SIMULATION SETUP

The initial density $n_0$ and magnetic field $\mathbf{B} = B_0[\mathbf{e}_y \sin\theta + \mathbf{e}_z \cos\theta]$ are uniform, and distribution function for each species is a drifting Maxwellian with uniform temperature $T$ and drift speed $\mathbf{U} = U_0 \tanh(x/L_V)\mathbf{e}_y$. Here, $L_V$ is the shear layer half-thickness and $U_0$ is the shear velocity. The initial electric field corresponding to the cross-field flow is $\mathbf{E} = -(B_0 U_0/c)\tanh(x/L_V)\mathbf{e_x}$. To support this field, a small number of excess electrons is loaded in the initial equilibrium with density $n_e(x)$ such that $\partial_x E_x = -4\pi e n_e(x)$. Periodic boundary conditions are imposed in $y$. The boundary conditions at $x = 0$ and $x = L_x$ are conducting for electromagnetic field and reflecting for particles. With the exception of comparison of the two runs at $\theta = 0^\circ$, and $\theta = 2.86^\circ$, all the 2D results shown in this paper are from our largest 2D simulation with plasma $\beta = 16\pi n_o T/B_0^2 = 0.1$, $L_V = 4d_i$, $m_i/m_e = 100$, $\theta = 2.86^\circ$, and $U_0 \approx 10V_A^*$, and $\omega_{pe}/\Omega_{ce} = 2$ where $\omega_{ce} = eB_o/(m_e c)$ and $\omega_{pe}^2 = 4\pi n_0 e^2/m_e$. This corresponds to strongly growing regime of Kelvin-Helmholtz instability (KHI).[31–33]

The initial electron and ion temperatures are equal $T_i = T_e = T$, $d_s = c/\omega_{ps}$ is the inertial length of species $s$ with mass $m_s$, and $V_A^* = B_0 \sin(\theta)/\sqrt{4\pi n_0 m_i}$. The simulation was performed in a rectangular domain in $x$-$y$ plane of size $L_x \times L_y = (50 \times 100)d_i$ and utilized a uniform computational grid with $8192 \times 16384$ cells corresponding to cell size of approximately 0.77 Debye length ($\lambda_D$). The simulation used 150 particles of each species per computational cell corresponding to approximately $4 \times 10^{10}$ total particles. We normalize time to $\Omega_{ci} = eB_0/(m_i c)$. The characteristic time for attaining the nonlinear phase is related to growth of the dominant Kelvin-Helmholtz mode. Since the fastest growth rates are of order $\gamma \sim \frac{1}{10} U_0/L_v \sim \Omega_{ci}/80$, nonlinearity is expected to dominate the dynamics after $t\Omega_{ci} \sim 80 - 160$. To expedite the initial growth of the KHI, the system is seeded with small perturbation of the flow of the form $\delta\mathbf{U} = \delta U_0 \sin(0.5y/L_V)\exp(-x^2/L_V^2)$, where $\delta U_0 = 0.15U_0$. We have carried out a parameter study for a range of $\beta$(0.1 to 1), $L_V$(0.5 to 4 $d_i$), $U_0$(2–20 $V_A^*$), $m_i/m_e = 25 - 500$, and $\theta = 0^\circ - 15^\circ$. Both 2D and 3D simulations were performed. A brief discussion of 3D and beta effects is provided in Sec. VII where we consider a simulation with $\beta = 2$, $m_i/m_e = 25$, $T_i/T_e = 3$, $\omega_{pe}/\omega_{ce} = 2$, $L_V = 2d_i$, $U_0 = 2V_A^*$, system size of $L_x \times L_y \times L_z = 50 \times 50 \times 100 d_i$, with $992 \times 992 \times 1984$ cells, and $\theta = 2.86^\circ$. A detailed discussion of the parameter dependency of the results will be considered elsewhere.

## III. TRANSITION TO TURBULENCE

The initial set up consists of uniform density, magnetic field, and an imposed velocity shear. The system evolves in three phases (Figure 1). First, the KHI grows linearly to form large-scale vortices. As vortices roll up, they wrap the in-plane magnetic field, giving rise to current sheets that are initially thicker than kinetic scales but comparable in length to the vortex structure. In time, these current sheets get compressed to the electron inertial scale ($d_e$),[34] triggering secondary tearing instabilities (Figure 1(b)) which are reasonably well described by linear theory (see Sec. III A) and KH instabilities. The fully developed turbulent phase (Figure 1(c)) involves continual formation and breakup of kinetic scale current sheets and magnetic islands. Hierarchy of coherent structures is clearly evident (Figure 1(d)) in close up of a region marked with a rectangle in Figure (1(c)). The size of each minor tick mark in Fig. 1(d) corresponds to $2d_e$. There is a suggestion of current sheet clusters of dimension $\sim d_i$, with individual sheet structures comparable to $d_e$. This phase shows qualitative similarities to fluid simulations of turbulence driven by the nonlinear interaction of Alfvén

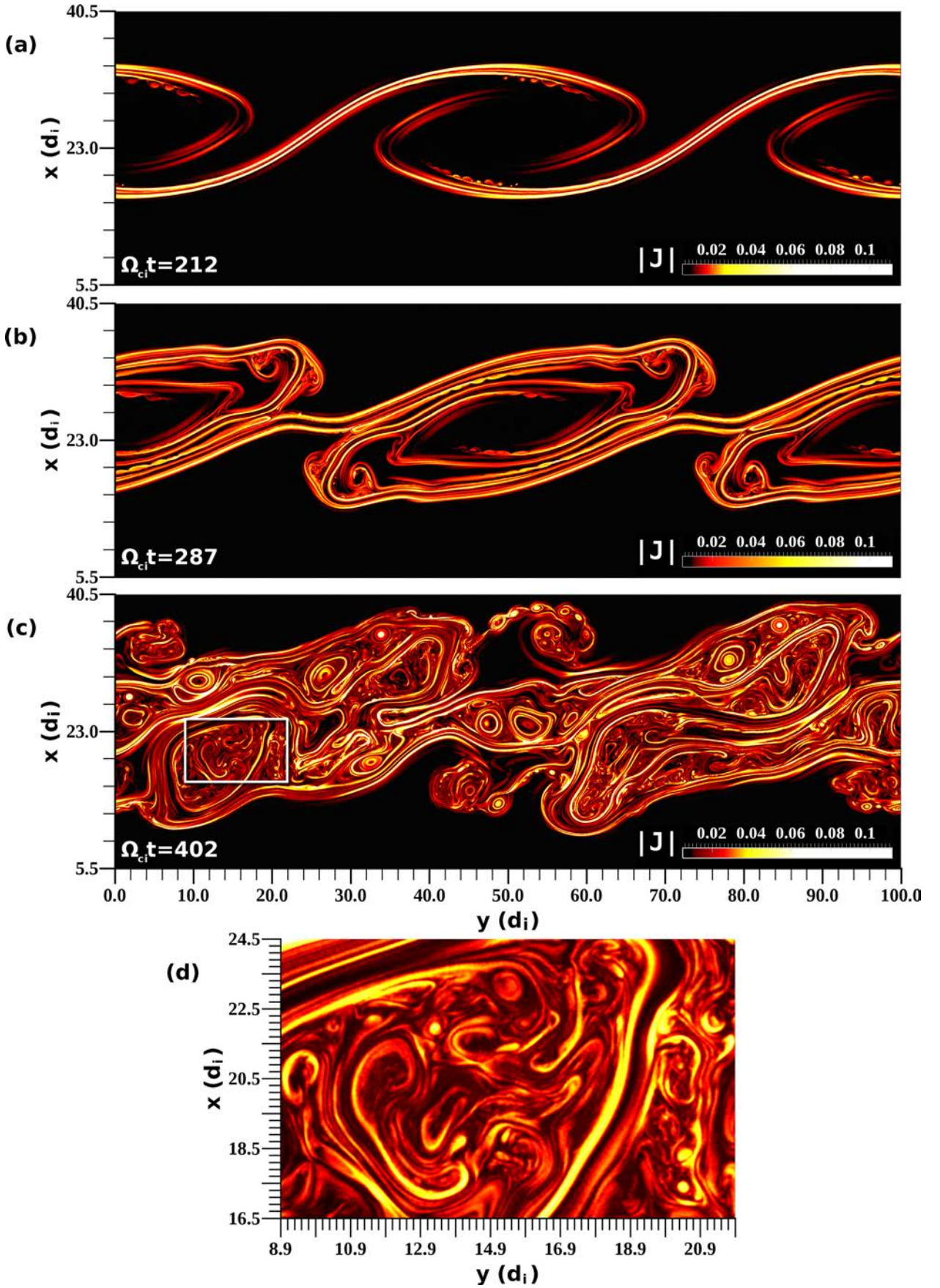


FIG. 1. Development of turbulence in physical space. (a) Formation of current sheets on the edge of the vortex. Current is normalized to $en_0c$. (b) Wrapping of current sheets inside the vortex and continuation of secondary instabilities. (c) Full development of turbulence. (d) Hierarchy of coherent structures as seen in close up of a region marked with a rectangle in (c). The size of each minor tick mark in Fig. 7(d) corresponds to $2d_e$.

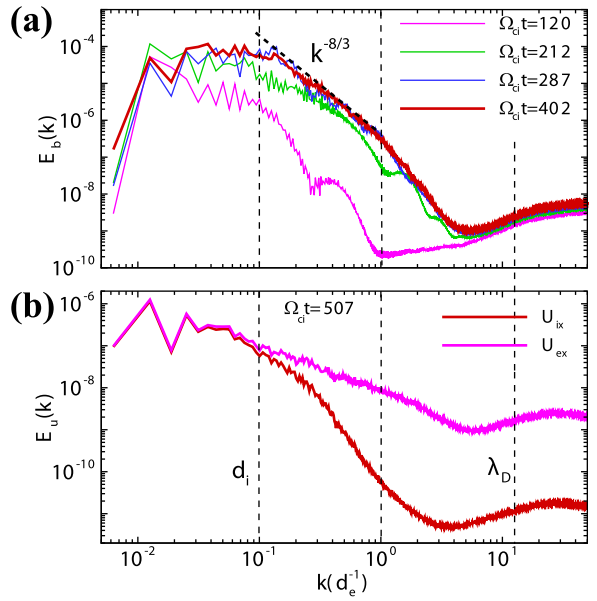


FIG. 2. (a) and (b) Omnidirectional energy (per unit mass) spectra of magnetic field and ion velocity field (Units not equated). Vertical dashed lines correspond to $d_i$, $d_e$, and Debye length $\lambda_D$, respectively. The magnetic spectra above $k = 1/d_i$ show several point spectral features.

waves.[4,35] However, the physics at kinetic scales is rigorously described within these fully kinetic simulations, allowing us to identify the physical origins of the resulting dissipation. This similarity is, however, highly suggestive that current sheet formation may be a generic feature of plasma turbulence in magnetized plasmas.

Figures 2(a) and 2(b) show the omnidirectional energy (per unit mass) spectra of magnetic field and ion velocity field (units not equated). Vertical dashed lines correspond to $d_i$, $d_e$, and Debye length $\lambda_D$, respectively. The magnetic spectra above $k = 1/d_i$ show several point spectral features. There is a strong feature (local maximum) near $kd_i = 3 - 4$ at $\Omega_{ci}t = 120$, and then at $\Omega_{ci}t = 220$ a pair of weaker features around $kd_e \approx 1.75$ and at $kd_e \approx 3$. The first of these is near the reciprocal ion gyroradius $\rho_i = d_i\sqrt{\beta} \sim d_i/\sqrt{10}$, and the latter features lie between $kd_e = 1$ and $k\rho_e = 1$. These appear as the higher wavenumbers begin to "fill in," and suggest a role of ion gyroresonant and possibly electron gyroresonant effects during the transition to turbulence. These processes may contribute later as well, but these spectral features are completely washed out in the fully turbulent state.

### A. Excitation of secondary instabilitites

The evolution of the system is marked by continual formation of coherent chains of magnetic islands late into the simulation. The secondary tearing instabilities play an important role during transition as well as in the final state of the system. The onset of tearing caps how thin the current sheets can become as they are compressed due to the vortex roll-up. The resulting generation of magnetic islands also contributes to the intermittent nature of turbulence.

To illustrate the local instability origin of these chains of islands, we recall that reconnection and its linear antecedent, the tearing mode, are expected to localize in regions where the in-plane magnetic field reverses direction across a layer. In the 2D simulations, one can quickly identify these regions by plotting $B_i^{-1} = (B_x^2 + B_y^2 + \epsilon)^{-1/2}$ where $\epsilon \sim 10^{-6}$ is small number to keep the result finite. Large values of $1/B_i$ along an extended line are a necessary condition to develop tearing. The next requirement is to have sufficient magnetic shear and thin enough current sheets so that tearing mode can grow rapidly compared to convective times of the flow. Figure 3(a) shows a close up region of simulation at $\Omega_{ci}t = 287$ (a full-scale panel at this time was shown in Fig. 1(b)) that highlights the presence of two chains of islands. Comparison with Figure 3(b) shows that the location of these islands coincides with regions of weak $B_i$. Since we are interested in calculating the growth of the tearing before it forms magnetic islands, we consider the two current sheets the location of these islands at slightly earlier time $\Omega_{ci}t = 280$. The thickness of these two sheets is about $1.5d_e$ and their magnetic shears are about 14° and 11°, respectively. The wavelengths of the islands are measured to be $k\lambda \sim 0.4$ and 0.5, respectively. These estimates compare well with the wavelength of the fastest growing linear tearing mode which is $k\lambda = 0.5$ in thin kinetic-scale layers. Using a standard Harris equilibrium growth rate

$$\frac{\gamma}{\Omega_{ci}} = \frac{1}{\sqrt{\pi}}\left(\frac{\rho_i}{\lambda}\right)^3\left(\frac{m_eT_e}{m_iT_i}\right)^{1/2}\left(1+\frac{T_e}{T_i}\right)[1-(k\lambda)^2]\frac{B_{zo}}{B_{yo}}, \quad (1)$$

and measured parameters near the island chain, we estimate a tearing growth rate of $\gamma/\Omega_{ci} \sim 0.17$. The visible lifetime of the chain is about $\sim 20\Omega_{ci}^{-1}$, corresponding to a growth factor of $e^{3.4} \sim 30$ from the seed level, thus verifying that an interpretation as a secondary instability is reasonable. We repeated this analysis for other chains of islands emerging in the simulation and in all cases, even during the fully developed turbulent phase such as that in Figures 3(c) and 3(d), we have found a similar level of feasibility. Note that the chain of islands is generated within a secondary KH vortex in Fig. 3(c). This illustrates the self-similar nature of the observed turbulence. We emphasize that the linear stability analysis presented here should only be taken as indication of the presence of local instabilities in the soup of developing turbulence rather than implying that the modes are truly linear.

### B. Wave excitation

A variety of electromagnetic waves have been inferred to be present in the solar wind. The origin of these waves and their possible role in providing the necessary dissipation in the solar wind remain quite controversial and are beyond the scope of the present study. The most commonly assumed mechanism for generation of kinetic scale waves in the solar wind is the homogeneous cascade process. However, our present simulations provide an interesting possibility for excitation of waves due to the motion of coherent structures. Indeed, large scale turbulent motions cause perturbations that propagate away as electromagnetic waves, as shown in Figure 4. This direct wave generation can be significant because (a) it provides a means to generate waves that would not be possible through the commonly considered cascade process, and (b) the damping of these small amplitude waves can

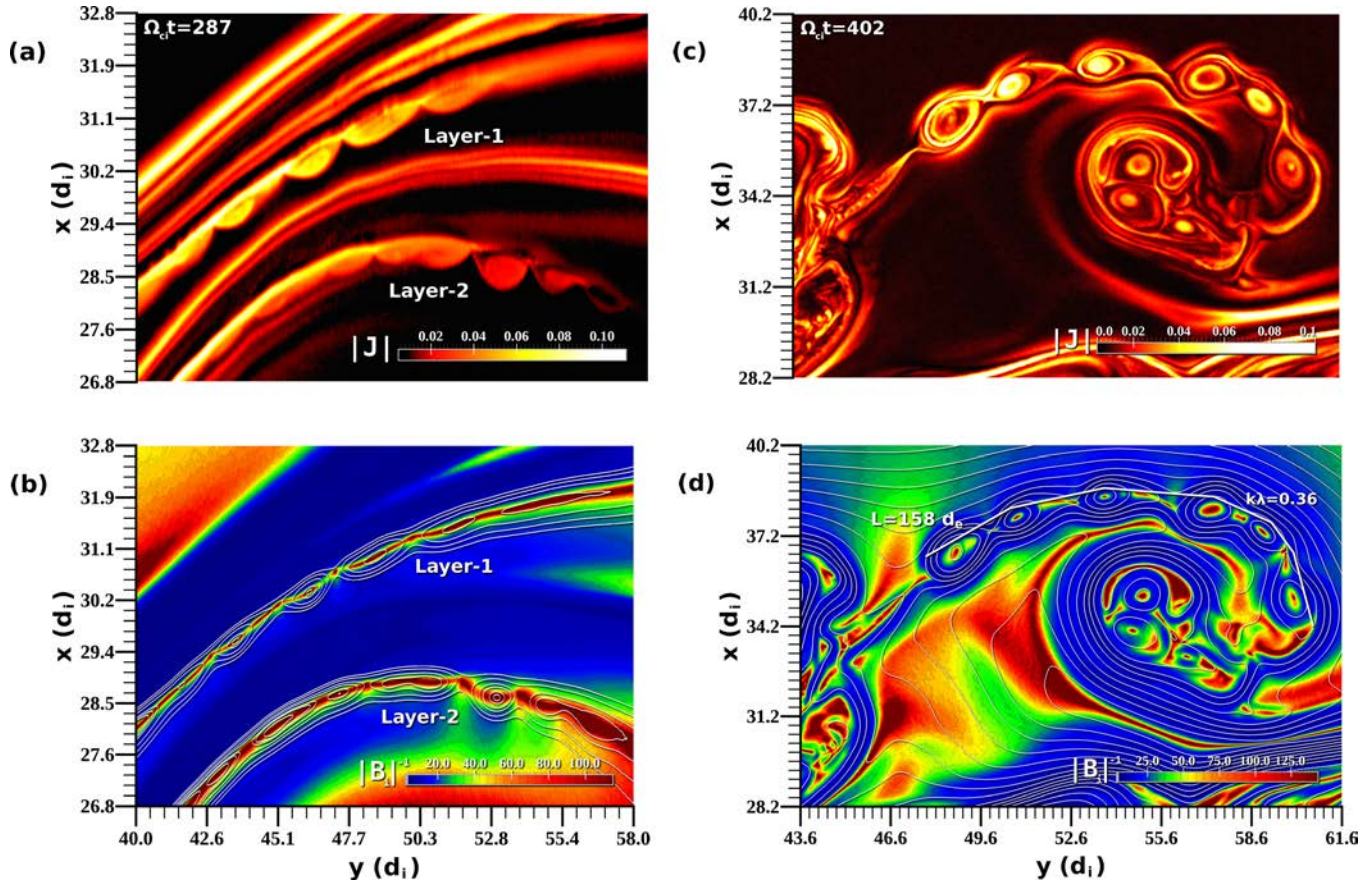


FIG. 3. Generation of secondary tearing instabilities. (a) Plot of $|J|$ showing the formation of chains of tearing islands at $\Omega_{ci}t = 287$. (b) Plot of $1/B_i$ highlighting the fact that tearing modes are formed in regions where the in-plane magnetic field is weak. Our linear tearing analysis was conducted for the two current sheets associated with these two chains of islands. Also shown are contours of vector potential $A_z$. (c) Plot of $|J|$ showing the formation of chains of tearing islands well into the turbulent phase at $\Omega_{ci}t = 402$ and (d) corresponding plot of $1/B_i$.

contribute to dissipation in regions between the current sheets. In order to identify the observed fluctuations, we computed the spectrum $S(\omega, k_x, k_y) = |B(\omega, k_x, k_y)|^2$ by performing fast Fourier transform (FFT) over time interval $200 < \Omega_{ci}t < 400$ in the edge of the simulation domain $40d_i < x < 50d_i$. Figure 5(a) shows the spectrum of $|B|^2$ for $k_x = 0$. Negative frequencies correspond to propagation in the $y$ direction. Overlay of the linear dispersion shows the presence of two modes, highly oblique magnetosonic mode (compressional), and the shear-Alfven/kinetic Alfvèn branch. For each branch (compressional and shear-Alfven), two doppler-shifted modes are visible, propagating in the $\pm y$ direction. Note that in 3D, modes propagating at other angles including parallel propagating whistlers may be generated. The peak amplitude of these waves is small with maximum $\delta B/B_0 \sim 10^{-2}$ which is comparable to those inferred at such scales from spectral studies of the solar wind. Figure 5(b) shows the magnetic compressibility $\delta B_\parallel^2/\delta B^2$. Consistent with linear theory, the Alfvèn branch has very low compressibility whereas magnetosonic branch shows high compressibility.

## IV. CHARACTERISTICS OF THE FULLY DEVELOPED TURBULENCE

The broadband nature of the fluctuations and the development of the strong turbulence regime can be demonstrated

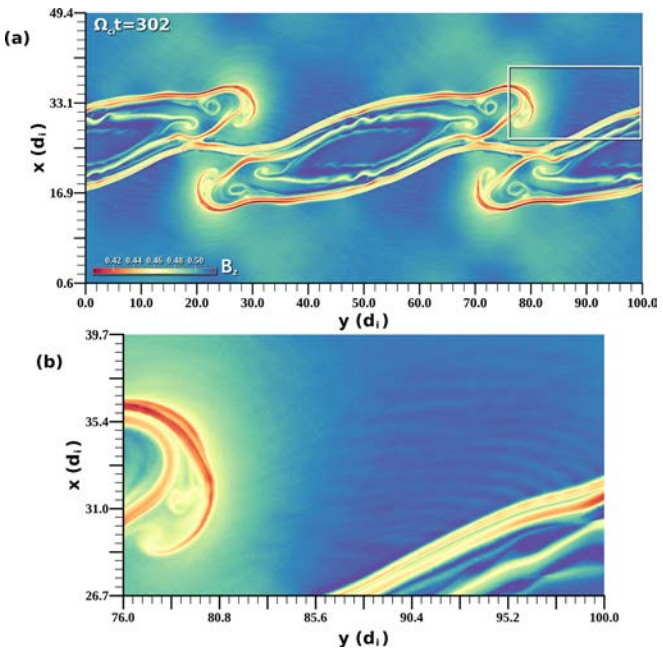


FIG. 4. Wave excitation. (a) Plot of $B_z$ illustrating the launch of waves into the ambient plasma. (b) Zoomed-in region marked with a box in (a).

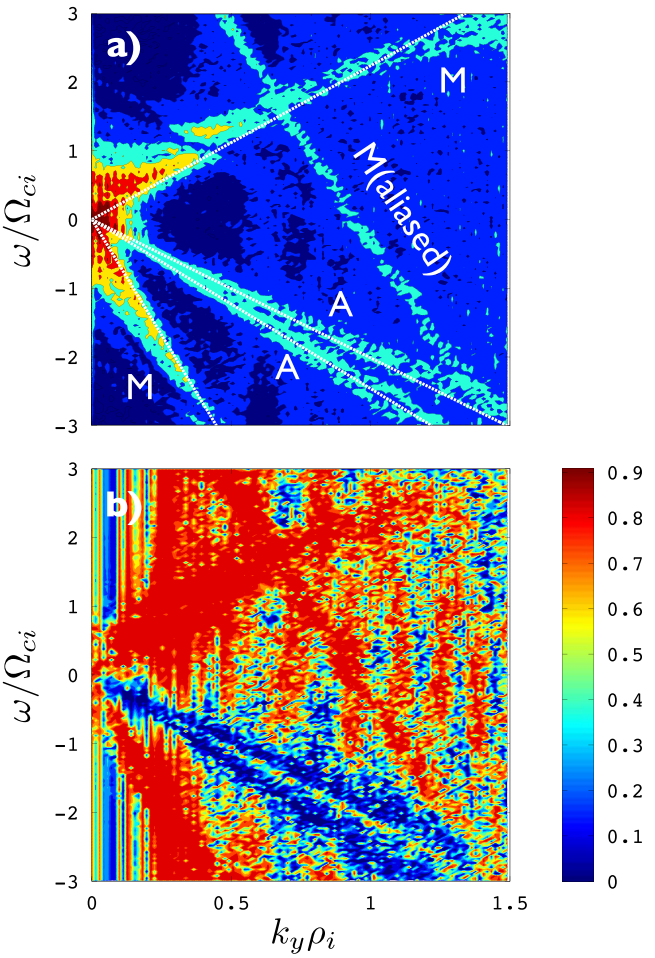


FIG. 5. Wave diagnostics. (a) Frequency vs $k_y$ spectrum of magnetic fluctuations computed at the edge of the simulation away from the vortex. Superimposed on the spectrum are lines corresponding to dispersion of compressional $k(U_0 \pm V_A)$ and shear Alfven modes $kU_0 \pm k_\parallel V_A$. (b) Compressibility diagnostic showing association of magnetosonic modes with high compressibility and shear Alfven modes with low compressibility as expected from the linear properties of these modes.

by the omnidirectional wavenumber spectra[36] of the cascading quantities (Figures 1(e) and 1(f)). For long wavelength scales $kd_i < 1$, the behavior is fluid-like and at sufficiently long times develops a Kolmogorov $k^{-5/3}$ spectrum. By $\Omega_{ci}t = 507$, and in the range $1/d_i < k < 1/d_e$ the magnetic spectrum has steepened to approximately $k^{-8/3}$. This is a power law frequently reported in solar wind studies in this range of scales.[22,23] For still smaller scales $kd_e > 1$ the spectra steepen further, although no clear power law is observed. Finally as $k$ approaches the reciprocal Debye scale, noise inherent in the PIC method becomes evident.

The ion fluid velocity spectrum $E_{Ui}$ (Figure 1(f)) at $\Omega_{ci}t = 507$ exhibits features similar to the magnetic energy spectrum at the same time. There is a break at or near $kd_i = 1$, and a somewhat less clear steepened range between $1/d_i$ and $1/d_e$. However, the spectrum of electron velocity $E_{Ue}$ is dramatically different. It traces $E_{Ui}$ until the wavenumber exceeds $kd_i \approx 0.6$ and thereafter $E_{Ue}(k)/E_{Ui}(k)$ monotonically increases until $kd_e > 1$. This is a clear manifestation of the onset of kinetic effects in a turbulent plasma at scales comparable to $d_i$, as is expected for low-$\beta$ regimes and is consistent with a recent study of spectral breaks in the power spectra of magnetic fluctuations in fast solar wind.[37]

Fourier spectral analysis cannot detect the presence of coherent structure visible in physical space shown in Figures 1(a)–1(d). However, a standard method in turbulence analysis[36,38] for quantifying the presence of coherent structures is the examination of probability distribution functions (PDFs) of the *increments* of the fluctuations. Dissipation in coherent structures is connected with non-Gaussian increment PDFs at small scales through the Kolmogorov refined similarity hypothesis (KRSH[39–41]). In hydrodynamics, the KRSH is well supported but unproven. As far as we are aware, a KRSH has not been formulated or tested for a kinetic plasma. The examination of the PDF of magnetic field increments (Figure 6) reveals the appearance of "extended tailed" PDFs on kinetic scales. The tails become more prominent as the spatial lag $s$ become smaller, down to the electron inertial scale $s = d_e$. Furthermore, the steepening of the spectra especially at $kd_e \sim 1$ suggests dissipation in this range of scales and this is consistent with the directly observed heating in the electron layers in physical space shown in Fig. 10. An unanticipated feature in this novel intermittency is that the fluctuations at still smaller scales, approaching $k\lambda_D = 1$, have a nearly Gaussian distribution. This is different than the intermittent cascade in hydrodynamics[39] and is most likely associated with the discrete nature of the PIC methodology but requires further study.

### A. Eddies in magnetized plasmas

"Eddies" may be defined as coherent patterns of velocity and vorticity (curl of velocity). Hydrodynamic turbulence is often viewed as made of an hierarchy of eddies over a wide range of scales. Another closely related concept is the "vortex" which is a region within a fluid where the flow exhibits mostly a spinning motion about an imaginary axis.

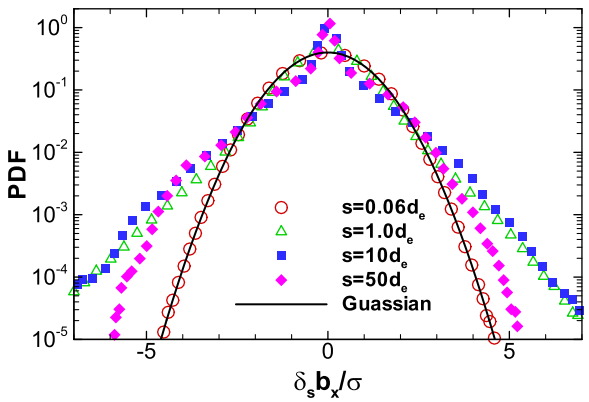


FIG. 6. Normalized PDF of magnetic field increments, where $\delta_s b_x = b_x(y+s) - b_x(y)$, and $\sigma$ is its variance. The increments are computed at spatial lag $s$, and as $s$ is decreased beginning with large (energy containing) scales, moving through inertial range scales, and into dissipative scales, the PDFs of velocity increments are found to become increasingly non-Gaussian, acquiring "extended tails" associated with enhanced occurrence of large nearly discontinuous jumps. This phenomenon is viewed as diagnostic of intermittency or burstiness of dissipation.

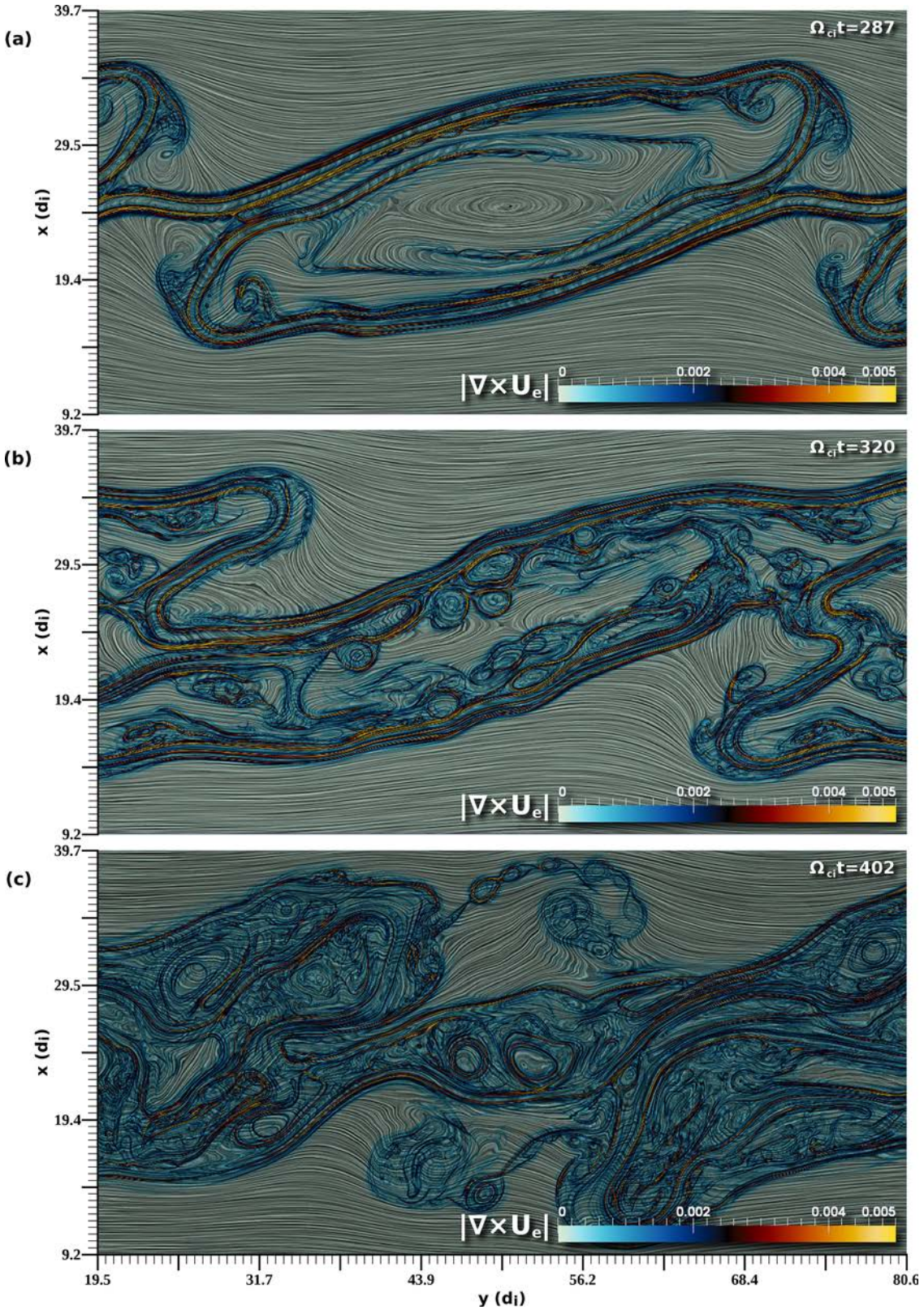


FIG. 7. Time evolution of the electron streamlines colored by the magnitude of the electron vorticity (a)–(c) and magnetic field lines colored by the magnitude of the field (d)–(f).

However, vortex is frame dependent and in a frame where the directional flow is much faster than the rotational speed, the vortex would not appear as such in the streamlines. In general, streamline patterns and vortex patterns differ in turbulence except near relaxed quasi-steady structures.[42] Here we show that similar to hydrodynamics, turbulence in plasma at kinetic scales causes the formation of eddies over the full range of scales from the initial size of the Kelvin-Helmholtz instability generated vortex and reaching down to electron length scales.

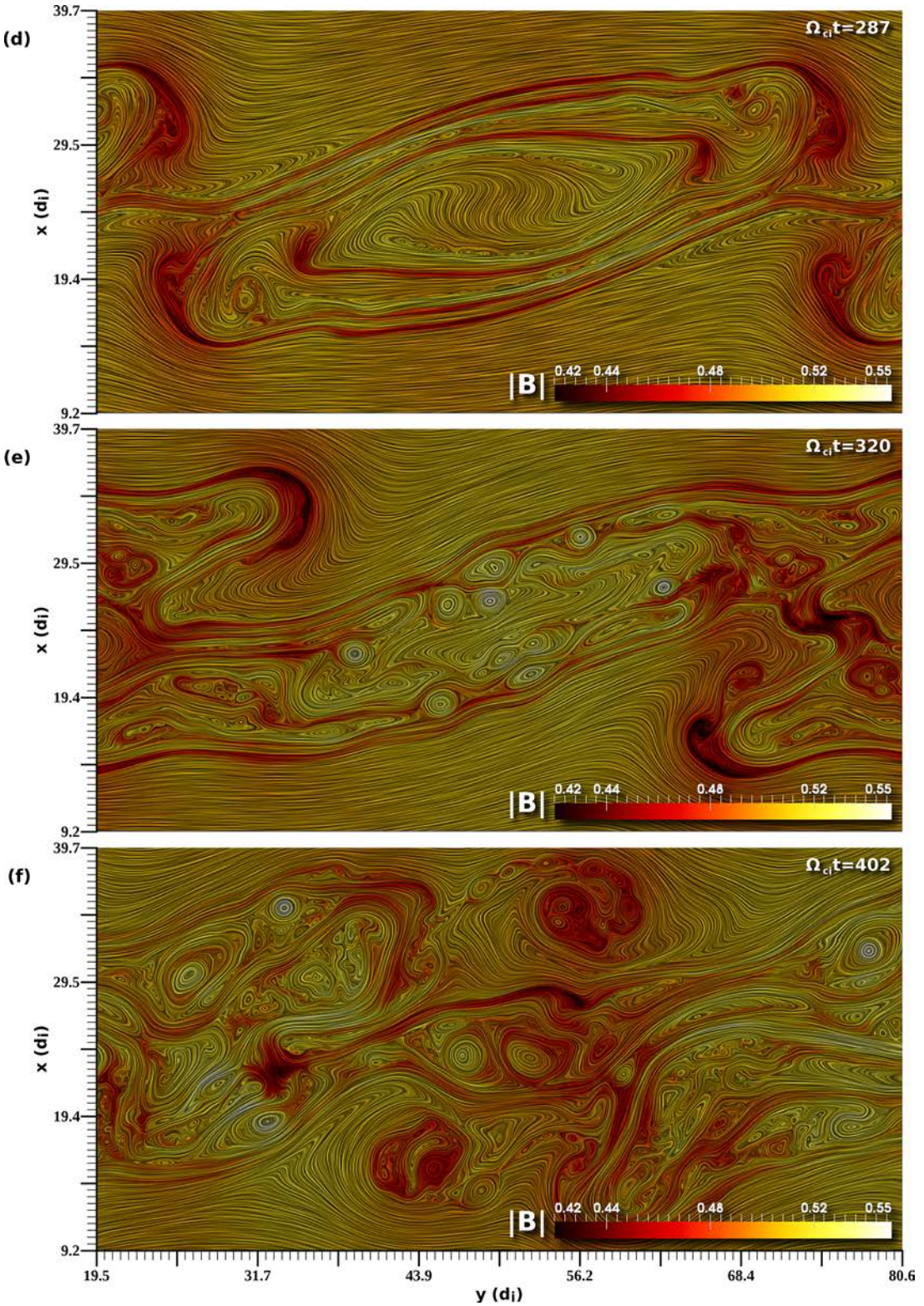


FIG. 7. (*Continued.*)

Because streamlines and lines of constant vorticity do not in general coincide, it is instructive to visualize them separately. Figures 7(a)–7(c) show the time evolution of the electron streamlines colored by the magnitude of the electron vorticity. The corresponding magnetic field lines colored by the magnitude of $B$ are shown in Figures 7(d)–7(f). Only a section of the simulation is shown. The line integral convolution (LIC) is a technique originally proposed to visualize fluid motion[43] and we have applied it here to visualize streamlines and magnetic field lines. Fig. 7(a) shows the presence of a vortical pattern in the center of the large vortex. Other smaller scale vortices are also apparent. Note that

the streamlines indicate flow into the current sheets in several regions. In time, a large number of vortices at a range of scales is generated as shown in Figs. 7(b)–7(c). Comparison of Figs. 7(a)–7(c) with Figs. 7(d)–7(f) reveals a strong correlation between electron vorticity structures, current sheets and magnetic islands. Fig. 7(d) shows that at this time the magnetic field near the center of the large vortex has not completely wrapped around. But in time, the magnetic field lines are distorted due to the repeated wrapping and multiple reconnections leading to the turbulent pattern seen in Figs. 7(e)–7(f).

## V. DISSIPATION MECHANISM

The powerful advantage of these kinetic simulations is that they allow us to study the details of the turbulent heating at the kinetic scales. Shear flow drives energy into bulk heating of particles, kinetic distortion of their distribution functions, current generation and amplification of in-plane magnetic field, and excitation of waves.

A time history of the changes in the energy budget (Figure 8) reveals a very efficient mechanism where about 30% of the initial energy in the flow has been converted into other forms. Of the 30% change in the ion flow energy, approximately 25% has appeared in the dynamically generated in-plane magnetic field energy, about 25% has gone into ion heating, and 50% is accounted for in electron heating.

Fig. 9(a) shows the electron velocity distribution at $t = 0$ and at the end of the run $\Omega_{ci}t = 507$, indicating that electrons are preferentially heated in the direction parallel to the magnetic field. This is consistent with the expected heating due to parallel electric fields generated in the reconnection process.[44] Energetic electrons constitute a small fraction of the energy partition. For example, 10% (1%) of the distribution resides at energies above 5 times (10 times) the thermal energy (Fig. 9(b)).

Figure 8(b) shows the comparison of change in ion flow energy for runs that are identical except for the presence ($\theta = 2.86^\circ$) or absence ($\theta$ is $0^\circ$) of an initial in-plane field. In the $0^\circ$ case, the vortex dynamics is decoupled from the magnetic field, and current sheet formation and reconnection are excluded. This severely limits the ensuing dissipation (a factor of 7 less) compared to the magnetically active case. However, this limit is not physical since in real applications, shear layers will always have some weak in-plane magnetic field, which can be amplified rapidly by shear.

In order to estimate the influence of numerical effects on the results, we performed simulations identical to the one used here, but with a limited number of cells in $y$ direction ($n_y = 100$) and the length reduced proportionally. KHI does not develop in this configuration and such simulations characterize the level of numerical dissipation. We have corrected results shown in this figure by the amount of numerical dissipation observed in the test runs. Furthermore, numerical heating of electrons is almost entirely in the in-plane direction, while the observed physical heating is preferentially in the out-of-the-plane direction. We note that the energy partition may be affected by many factors, such as

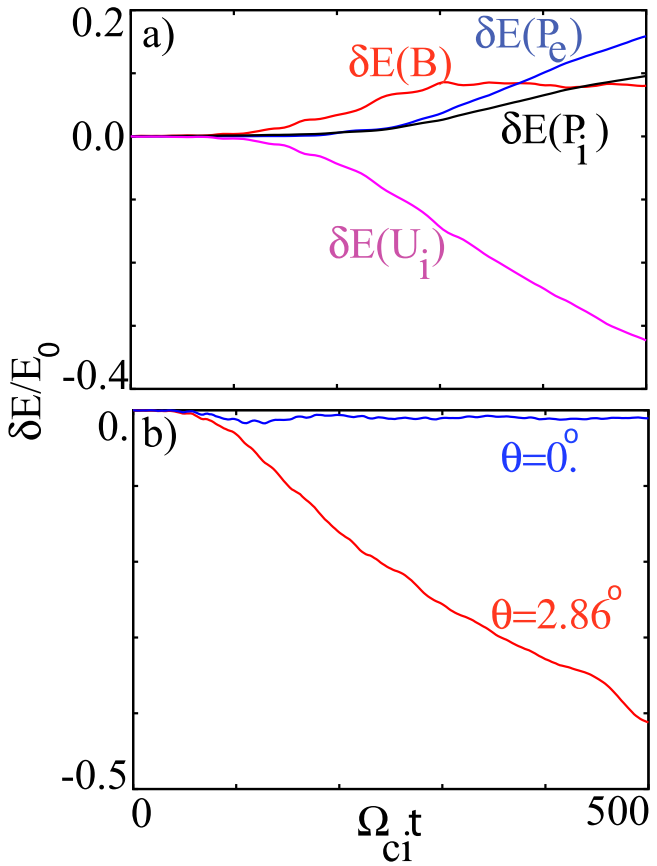


FIG. 8. $\delta E$ is defined to be the change in the energy for each component from its initial value. (a) Time evolution of changes from their initial value of energy of the electron thermal energy, ion thermal energy, in-plane magnetic field energy, and ion flow energy. (b) Comparison of change in ion flow energy for runs that are identical except for the presence ($\theta = 2.86^\circ$) or absence ($\theta$ is $0^\circ$) of an initial in-plane field.

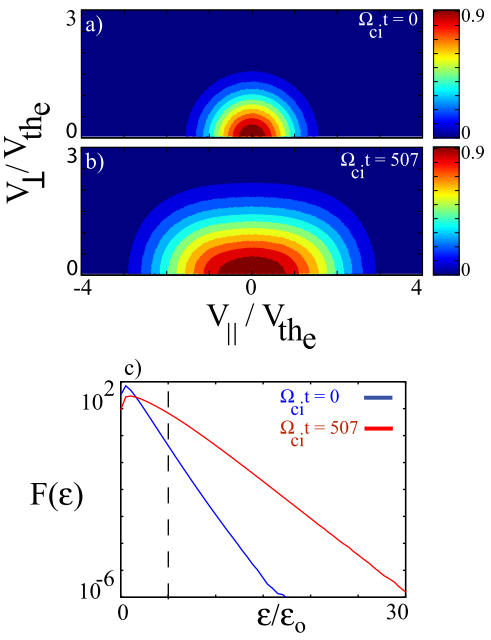


FIG. 9. Characterization of electron energization. (a) Electron distribution function in $V_{||} - V_{\perp}$ coordinates at $t = 0$ and $\Omega_{ci}t = 507$. Electrons are heated preferentially in the direction along the imposed magnetic field. (b) Electron energy distribution. The dashed line is drawn at 5 times the electron thermal energy as a way to define high energy portion of the distribution function.

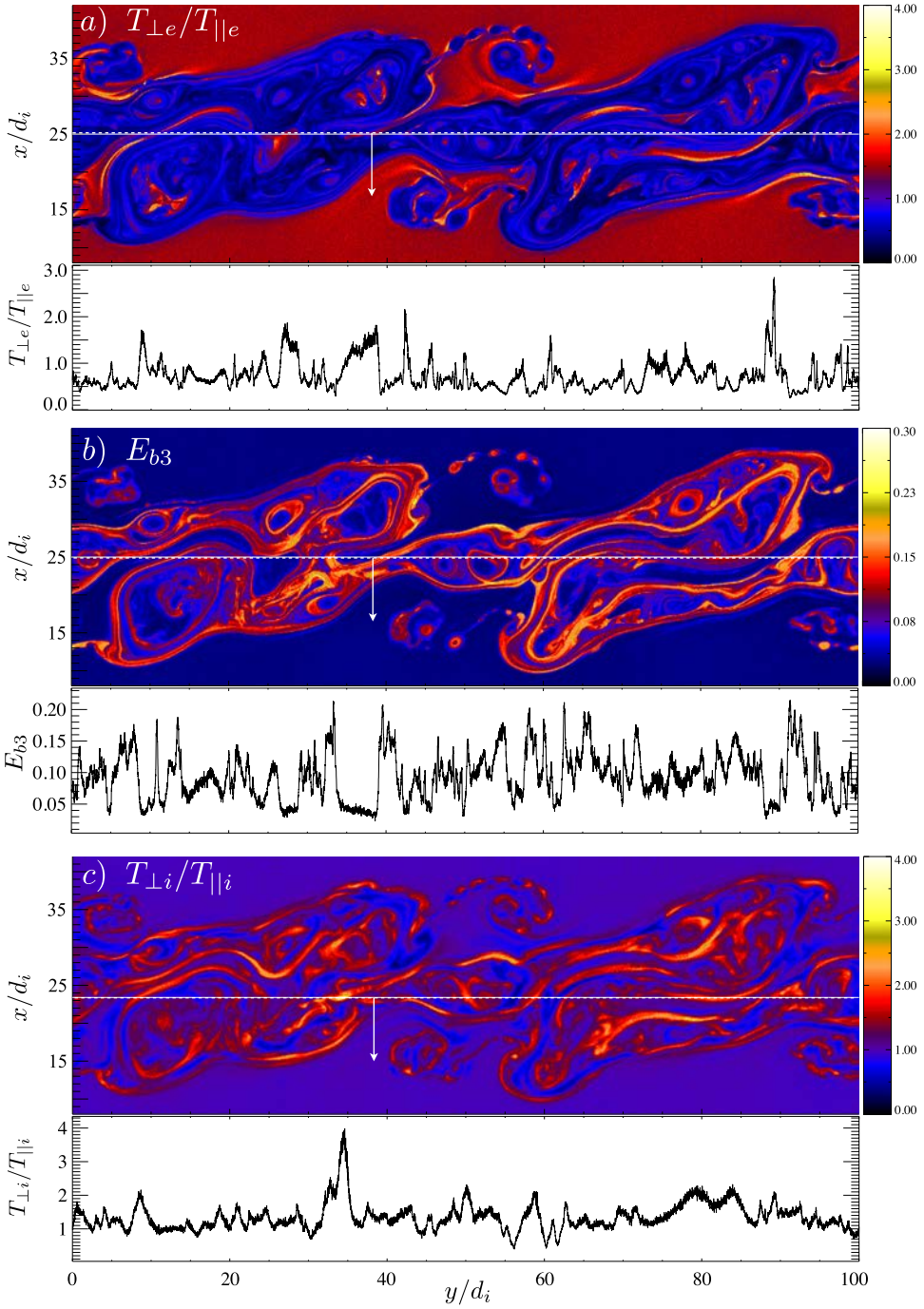


FIG. 10. Dissipation in localized structures. Filamentary structure of turbulence as may be seen by spacecraft. (a) Plot of electron temperature anisotropy and a 1D cut mimicking of what a spacecraft may see in crossing such regions. (b) Density of electrons with energy in the range of $(6-9)T_{e0}$ where $T_{e0}$ is the initial electron temperature. Energy band diagnostic consists of calculating the density of particles in each computational grid with energies in a preselected range of energy bands. (c) Ion temperature anisotropy.

values of $\beta$, $\omega_{pe}/\omega_{ce}$, and $m_i/m_e$. However, results shown here provide a reasonable estimate of the expected efficiency of conversion and partitioning of energy.

### A. Signatures of dissipation

A key signature of the dissipation mechanism is its highly inhomogeneous heating of electrons and ions as demonstrated in Figure 10. Our results provide testable predictions for the upcoming spacecraft observations. Figure 10 shows several diagnostics along with 1D cuts which show signatures that a spacecraft flying through such regions may detect. The turbulence also exhibits filamentary fluctuations in the ion temperature anisotropy as shown in Figure 10(c). High resolution instruments, such as NASA's upcoming Magnetospheric MultiScale, will have sufficient resolution to measure these features. Interestingly enough, the range of anisotropy seen here $0.5 < T_\perp/T_\parallel < 4$ is in good agreement with that seen in the solar wind.[45] We note that the formation of ion temperature anistropy has also been reported in study of plasma turbulence using the Vlasov hybrid approach.[13]

Figure 10(b) shows the density of electrons with energy in the range of $(6-9)T_{e0}$ where $T_{e0}$ is the initial electron temperature. Most of the energization is due to parallel electric fields and is seen to be closely associated with the thin current sheets ranging in scales from $d_i$ all the way down to $d_e$.

The finite electron anisotropy in region outside of the vortex is due to the usual numerical heating associated with particle codes which is predominantly in the perpendicular direction. This is consistent with the results of our thermal

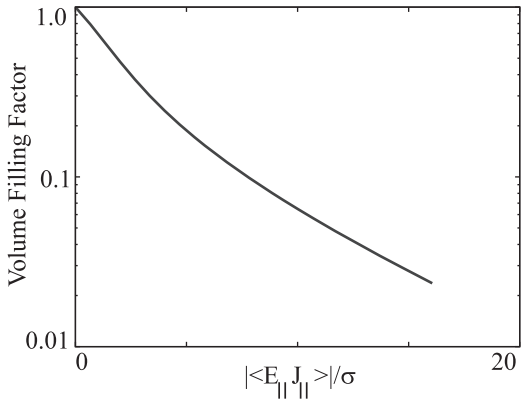


FIG. 11. Plot of the volume filling factor of coherent structures as measured by the volume of space that has $|\langle E_\parallel J_\parallel \rangle|$ exceeding a given threshold value on the x-axis. The x-axis is normalized to the noise level, i.e., standard deviation of $|\langle E_\parallel J_\parallel \rangle|$ in the quiet region of the simulation.

run which we used to assess the size of numerical heating in the run. The physical heating in the parallel direction is much larger than this perpendicular heating. The numerical heating makes it more difficult for the system to reach the fire-hose marginal condition $\beta_\parallel - \beta_\perp = 2$. However, in this low $\beta$ case, even accounting for this numerical heating, the system remains far from the fire-hose condition. At sufficiently high $\beta$, the current sheets may reach the fire-hose marginal condition which would tantamount to relieving the field tension. This in turn would enable the roll-up to proceed easier and secondary KH can be excited more readily. The mirror and Alfvèn ion cyclotron modes also have higher growth rates at higher $\beta$ and could be excited in such regimes.

One important question is how volume filling are the current sheets. The proper dissipation proxy for a kinetic plasma remains controversial. In a companion paper,[18] we used several proxies to quantify the details of the dissipation mechanism and its association with the current sheets. Here we use $E_\parallel J_\parallel$, which is related to the local rate of energy transfer between particles and electromagnetic field. Since a significant portion of the dissipated energy goes into parallel heating of the electrons, this quantity should represent a significant portion of the total dissipation rate. Figure 11 shows a plot of the volume filling factor versus $|\langle E_\parallel J_\parallel \rangle|$. Here, $\langle\rangle$ corresponds to time average over 200 time steps (approximately 0.6 of electron gyroperiod) to reduce noise. It is immediately apparent that the volume filling factor rapidly decreases with intensity, indicating localization of the dissipation inside coherent structures. For a rather conservative definition of significant dissipation $|\langle E_\parallel J_\parallel \rangle| > 5\sigma$, the volume filling factor is $\sim$ 20%. Here, $\sigma$ is the standard deviation measured in the region outside of the vortices.

Figure 12(a) shows threshold plot of $E_\parallel J_\parallel$ where values below 5 times noise level value are set to 0 (black) and those above are set to 1. Also shown is $|J|$ in Fig. 12(b). The correlation of $E_\parallel J_\parallel$ with current sheets is clearly evident in the overlay of the two images (Fig. 12(c)). We caution that accurate measurement of the volume filling factor is difficult as it is affected by particle noise and it also depends on the particular choice of the threshold value. However, the estimate here indicates that volume filling factor of current sheets is significant and larger than a few percent.

## VI. HEATING ESTIMATES

One important question is whether the observed rate of dissipation in the solar wind can be explained easily in turbulence theory, and whether the same explanation works in the present simulations. The expected decay rate associated with strong turbulence is obtained using the Taylor-von Karman

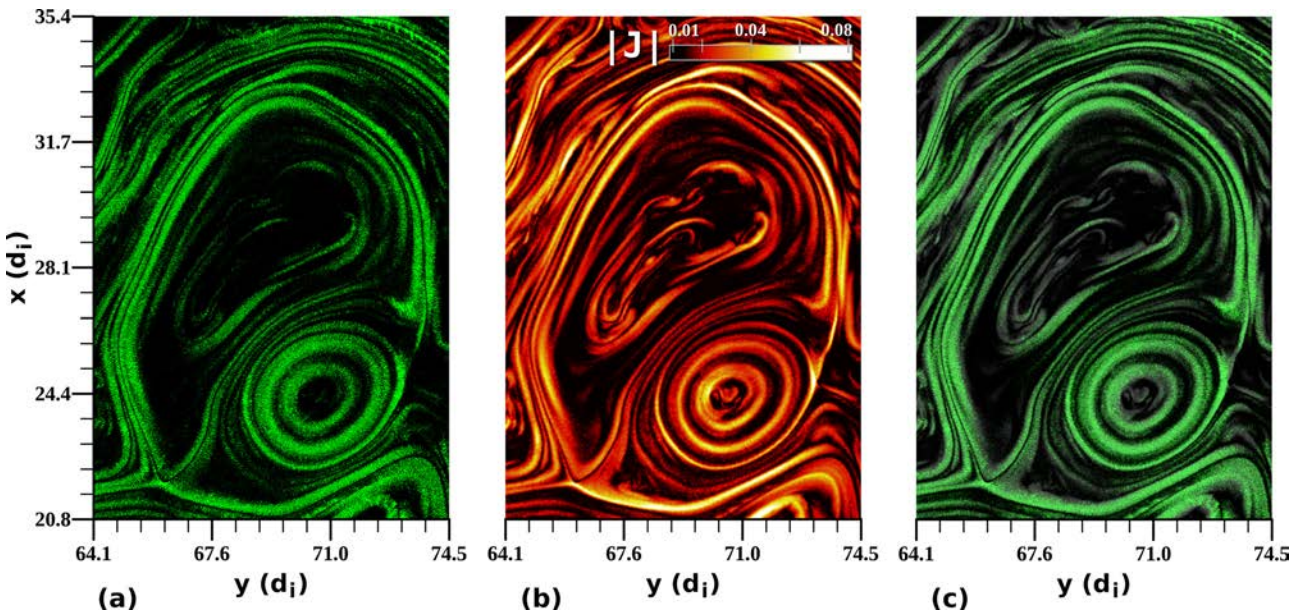


FIG. 12. (a) Threshold plot of $|\langle E_\parallel J_\parallel \rangle|$ where values below 5 times noise level value are set to 0 (black) and those above are set to 1. (b) Plot of $|J|$. (c) Overlay of the two panels, showing a close association of $E_\parallel J_\parallel$ with intense current sheets. Bandpass filter was used to remove grid-scale noise.

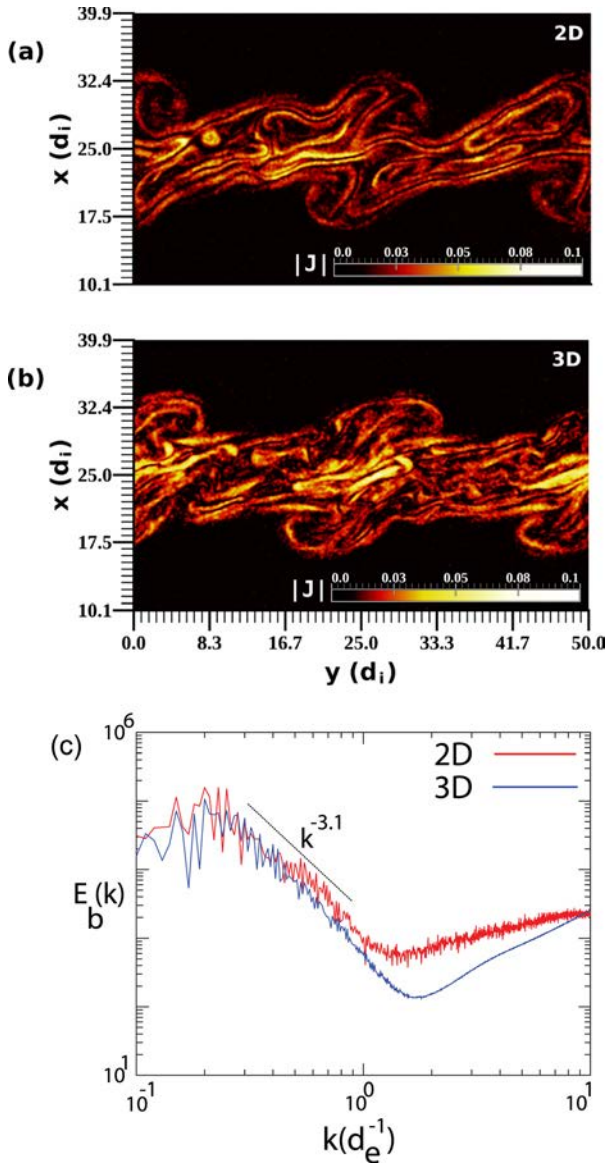


FIG. 13. 3D effects. Comparison of 2D and 3D simulations of shear driven turbulence at $\Omega_{ci}t = 99$. Intensity plot of the total current density in (a) 2D and (b) 3D. (c) Spectrum of the total magnetic energy in 2D (red) and 3D (blue), showing similar spectral index of ~3.1. The 2D result has been rescaled to match total magnetic energy in 3D.

estimate $\epsilon \sim U^3/L$ for appropriately chosen similarity scale $L$ and turbulence amplitude $U$. For solar wind near 1 AU, we adopt typical values $L \sim 10^6$ km and $U \sim 20-30$ km/s,[28] leading to $\epsilon \approx 8000-27000$ J/kg s. On the other hand direct examination of the steady solar wind temperature equation at (1) AU (Ref. 46) gives $\epsilon \sim 2400$ J/kg s, while various studies employing the theoretically appealing but statistically delicate MHD third-order law (see Ref. 47 for a summary) have given results in the range of $200-8000$ J/kg s. Given the level of variability of solar wind at 1 AU, this level of agreement is supportive of a turbulence heating scenario.

It is important to note that the Taylor-von Karman estimate can also be used to explain the observed rate of dissipation in our simulation. For the current simulation, the decay of energy indicates a sustained energy decay rate for $\Omega_{ci}t > 220$ of $\epsilon \sim 10^{-9}$ $c^3/d_e$. To compare with turbulence theory, we employ $L \sim 200d_e$ and conservatively estimate the turbulence amplitude using the magnetic fluctuation energy, leading to the estimate $\epsilon \sim (\delta V_A^3/L) = 4 \times 10^{-9}$ $c^3/d_e$. In the simulation, as in the solar wind, the turbulence decay rate which does not depend on the properties of individual microscopic events (but does rely on presence of a plethora of such events) is roughly consistent with the directly measured heating rate.

## VII. 3D AND BETA EFFECTS

The relative importance of 2D versus 3D depends on the type of turbulence. For example, the turbulent cascade of Alfvenic fluctuations is an inherently three-dimensional process because Alfvenic fluctuations require variation along the magnetic field to propagate, and the dominant nonlinearity requires variation in both directions perpendicular to the magnetic field.[10] In contrast, the essence of shear driven turbulence remains similar in 2D and 3D. To illustrate this point, we show in Figs. 13(a) and 13(b) the comparison of the total current density in $x-y$ plane from a 2D and a slice in $z$ of a 3D simulation. The parameters are $\beta = 2$, $m_i/m_e = 25$, $T_i/T_e = 3$, $\omega_{pe}/\omega_{ce} = 2$, $L_V = 2d_i$, $U_0 = 2V_A^*$, system size of $L_x \times L_y \times L_z = 50 \times 50 \times 100d_i$, with $992 \times 992 \times 1984$ cells, 150 particles per cell per species, and $\theta = 2.86^\circ$. Note that the plasma beta is a factor of 20 larger in this run than in the 2D run that we highlighted in other sections. However, the basic processes in the transition to turbulence and many of the details of turbulence remain similar to that at lower beta. The thickness of the currents in 2D and 3D is comparable and has a minimum scale of an electron skin depth. A comparison of the spectrum of the total magnetic energy is shown in Figure 13(c) which again shows that in this problem 2D (red) and 3D (blue) evolutions are not drastically different.

One interesting difference between 2D and 3D is that in 3D a broader range of instabilities can be excited. In 2D as in Figure 3, many of current sheets do not permit tearing because the resonance surfaces would be out of the plane of the simulation. However, in 3D all of the current sheets would allow tearing. Furthermore, new instabilities such as lower hybrid drift instability may be triggered in 3D which could in turn broaden the current sheets to several electron skin depths and kink the current sheets.[48] We will discuss these complications in a future publication.

## VIII. DISCUSSION AND SUMMARY

In turbulence, energy is often supplied by gradients at large scales, and cascades through nonlinear interactions to small scales where the collective motions are dissipated into heat. A question of substantial importance in extending classical turbulence theory to these space and astrophysical plasmas is the identification of key dissipative mechanisms that transform cascade energy into heat. While large scale motions are well described by fluid theory, the interface between fluid motions and kinetic plasma dynamics, and the

details of the dissipation process, remains enigmatic. However, the advent of petascale supercomputers has now made it possible to reveal these features through fully kinetic simulations that span the range of scales from fluid to kinetic range. Here, we reported on the first results from these simulations with a focus on the solar wind turbulence problem where the availability of *in situ* spacecraft measurements provides stringent constraints on the results. Starting with a laminar, large scale velocity shear, the fluid-scale cascade drives a strongly nonlinear kinetic cascade characterized by a hierarchy of dissipative coherent structures extending down to electron scales. The cascade is punctuated by secondary tearing and Kelvin-Helmholtz instabilities. The largest percentage of the dissipated energy is found to go into heating of electrons and ions with progressively smaller percentages going into magnetic field generation, production of energetic particles, and excitation of waves (highly oblique magnetosonic waves). The main heating mechanism is associated with anisotropic electron heating in current sheets, and is reminiscent of collisionless magnetic reconnection, with much weaker heating associated with the waves.

Another interesting finding is that the motion of coherent structures, including the vortex and the embedded magnetic islands, leads to emission of waves that propagate away from the vortex region. This is analogous to sound wave generation due to turbulent fluid motion in aeroacoustics.[30,36] This wave mechanism has not been considered in the solar wind and may lead to generation of waves that may otherwise not be possible. The properties of such waves would be related to the size and speed of the coherent structures. In most cases, the waves are expected to remain at small amplitudes. But we have verified that for high enough Mach number, the waves steepen and form shocks. However, regardless of the source of waves, the dissipation efficiency due to waves is several orders of magnitude smaller than that due to reconnection as a simple estimate demonstrates. We compare the energy gain of a particle from interacting with a wave versus a reconnection site. The potential of a KAW $\Phi_{KAW}$, a leading candidate in wave damping models, is given by (see Appendix) $e\Phi_{KAW}/T_e \sim (1/\sqrt{\beta_i(1+\beta_i)}(\delta B/B_0)$. Here, $\delta B$ is the wave amplitude, $q_i = e$, and we have assumed $T_i = T_e$. The potential due to magnetic reconnection is $e\Phi_{rec}/T_e \sim 1/\sqrt{\beta_e}$ for moderate values of electron beta[44] $\beta_e > 0.01$. Here for simplicity, we have neglected other mechanisms of heating associated with current sheets such as heating of ions due to the perpendicular electric field. Thus we get $\Phi_{KAW}/\Phi_{rec} \sim \delta B/B_0 \sim 0.01$, where we have used inferred wave amplitude at kinetic scales in the solar wind.[22,23] This indicates that the energy gain due to reconnection in the electron layers is at least ~100 larger than that due to KAW. This means that coherent accelerating regions can be at least a factor of 100 less volume filling (~1%) than waves and still yield comparable heating. This estimate is remarkably consistent with an observation in the magnetosheath where direct measurement of damping rate from reconnecting current sheets was found to be a factor of ~100 larger than the wave damping rate.[49] Note that the volume filling factor is over 20% in the present case (Fig. 11(a)). It is interesting to note that in regimes with $\beta_i < 1$, the potential for KAW and reconnection scale in the same manner ($\Phi_{KAW} \propto 1/\sqrt{\beta_i}$, $\Phi_{rec} \propto 1/\sqrt{\beta_e}$) implying the relative efficiency is nearly independent of $\beta$ for a fixed temperature ratio $T_i/T_e$.

These results are highly suggestive that in description of solar wind and other plasmas like the interstellar medium, discussion of physics of the cascade needs to go beyond the simple phenomenology for the spectral laws. The total dissipation rate is expected to be set by the large-scale drive. We have in fact verified that in the simulation, as in the solar wind, the turbulence decay rate is roughly consistent with the directly measured heating rate (Sec. VI). These two estimates indicate that the cascade into current sheets and the ensuing strong heating is sufficient to explain the observed heating rates in the solar wind.

The first-principle simulations here pave the way for future studies of turbulence, collisionless dynamo, and MRI. We have already started on 3D fully kinetic simulations of wave turbulence and will report the results elsewhere. Our preliminary results suggest that electron scale current sheet generation may be a generic feature of collisionless turbulence.

## ACKNOWLEDGMENTS

This work was partially supported by DE-SC0004662, NASA through the Heliophysics Theory Program and NNH11CC65C, and NSF through EAGER 1105084. The Delaware group (W.H.M., M.W., P.W., and M.S.) is supported by NASA (Heliophysics Theory NNX11AJ44G, Solar Probe Plus and MMS Theory programs) and by NSF (AGS-1063439 and SHINE AGS-1156094). S.C.C. acknowledges support from the UK EPSRC and STFC. Simulations were performed on Kraken provided by the NSF at NICS, on Pleiades provided by NASA's HEC Program, and resources of the National Center for Computational Sciences at Oak Ridge National Laboratory (Jaguar/Lens), which is supported by DOE under Contract No. DE-AC05-00OR22725. Visualization and analysis were performed on Nautilus and Longhorn systems using ParaView and visualization software developed by the NICS RDAV group. We acknowledge useful conversations with J. TenBarge on kinetic Alfvén turbulence. We also thank the referee for useful comments that led to improvements in the paper.

## APPENDIX: CALCULATION OF PARALLEL ELECTRIC FIELD OF KINETIC ALFVÉN WAVES

In general, $\mathbf{E} = -\nabla\Phi - (1/c)\partial\mathbf{A}/\partial t$, therefore

$$E_\parallel = -\nabla_\parallel \Phi - \frac{1}{c}\frac{\partial A_\parallel}{\partial t}. \tag{A1}$$

Fourier transforming equation (1) yields

$$E_\parallel = -ik_\parallel \Phi + \frac{i\omega_k}{c} A_\parallel. \tag{A2}$$

The simplest expression for the kinetic Alfvén wave $E_\parallel$ can be derived from electron reduced MHD (ERMHD), which

is a generalization for electron MHD for low frequency, anisotropic fluctuations without assuming incompressibility. The linearized ERMHD equations yield frequencies[50]

$$\omega_k = \pm k_\parallel v_A k_\perp \rho_i \sqrt{\frac{1+Z/\tau}{2+\beta_i(1+Z/\tau)}} \tag{A3}$$

and eigenfunctions

$$\theta_k^{\pm} = \sqrt{\left(1+\frac{Z}{\tau}\right)\left[2+\beta_i\left(1+\frac{Z}{\tau}\right)\right]}\frac{c\Phi}{\rho_i B_0} \mp k_\perp \frac{v_A A_\parallel}{B_0} = 0, \tag{A4}$$

where $\tau = T_i/T_e$, $Z = q_i/|q_e|$, $\beta_i = v_{ti}^2/v_A^2$, $v_A^2 = B_0^2/4\pi m_i n_i$, $v_{ts}^2 = 2T_s/m_s$, and $\theta_k^{\pm}$ is equivalent to Elsasser fluxes in MHD.

For simplicity, we will take $Z = 1$. Finally, combining Eqs. (2)–(4), we find

$$E_\parallel = -ik_\parallel \Phi\left[1 \pm \left(1+\frac{1}{\tau}\right)\right] \simeq -ik_\parallel \Phi, \tag{A5}$$

where the latter equality follows from assuming $\tau \simeq 1$.

From Eq. (4), we have

$$\Phi = \frac{k_\perp \rho_i}{\sqrt{\left(1+\frac{Z}{\tau}\right)\left[2+\beta_i\left(1+\frac{Z}{\tau}\right)\right]}}\frac{v_A A_\parallel}{c}. \tag{A6}$$

The magnetic field can be expressed in terms of the parallel vector potential as $\delta \mathbf{B}_\perp = \hat{\mathbf{z}} \times \nabla_\perp A_\parallel$. Thus, we can express the electric potential in terms of a component of the magnetic field as

$$\Phi = \frac{k_\perp \rho_i v_A}{c k_y \sqrt{\left(1+\frac{Z}{\tau}\right)\left[2+\beta_i\left(1+\frac{Z}{\tau}\right)\right]}}\delta B_x. \tag{A7}$$

Normalizing to the electron thermal energy yields

$$\frac{q_i \Phi}{T_e} = \frac{2\tau k_\perp \rho_i}{\beta_i k_y d_i \sqrt{\left(1+\frac{Z}{\tau}\right)\left[2+\beta_i\left(1+\frac{Z}{\tau}\right)\right]}}\frac{\delta B_x}{B_0}. \tag{A8}$$

Assuming $\tau = 1$, and $Z = 1$, we obtain

$$\frac{q_i \Phi}{T_e} = \frac{k_\perp}{k_y}\frac{1}{\sqrt{\beta_i(1+\beta_i)}}\frac{\delta B_x}{B_0}. \tag{A9}$$

The potential of the wave is the maximum energy that the wave can impart to the particle if the wave was entirely dissipated. In practice, the energy gain is a fraction of this potential.


[1]P. Goldreich and S. Sridhar, Astrophys. J. **438**, 763 (1995).
[2]G. Zank and W. H. Matthaeus, Phys. Fluids A **5**, 257 (1993).
[3]A. Lazarian and J. Cho, Phys. Scr., T **116**, 32 (2005).
[4]P. Dmitruk and W. Matthaeus, Phys. Plasmas **13**, 042307 (2006).
[5]A. Beresnyak, Phys. Rev. Lett. **106**, 075001 (2011).
[6]P. Diamond, S.-I. Itoh, and K. Itoh, *Relaxation Dynamics in Laboratory and Astrophysical Plasmas, Vol. 1: Biennial Reviews of the Theory of Magnetized Plasmas*, edited by P. G. Patrick, H. Diamond, X. Garbet, and Y. Sarazin (World Scientific, 2009), pp. 117–150.
[7]A. V. Usmanov, M. L. Goldstein, and W. H. Matthaeus, Astrophys. J. **754**(1), 40 (2012).
[8]E. Lee, M. E. Brachet, A. Pouquet, P. D. Mininni, and D. Rosenberg, Phys. Rev. E **81**, 016318 (2010).
[9]T. N. Parashar, M. A. Shay, P. A. Cassak, and W. H. Matthaeus, Phys. Plasmas **16**, 032310 (2009).
[10]G. G. Howes, J. M. TenBarge, W. Dorland, E. Quataert, A. A. Schekochihin, R. Numata, and T. Tatsuno, Phys. Rev. Lett. **107**, 035004 (2011).
[11]O. Chang, S. P. Gary, and J. Wang, Geophys. Res. Lett. **38**, L22102, doi:10.1029/2011GL049827 (2011).
[12]D. Verscharen, E. Marsch, U. Motschmann, and J. Muller, Phys. Plasmas **19**, 022305 (2012).
[13]S. Servidio, F. Valentini, F. Califano, and P. Veltri, Phys. Rev. Lett. **108**, 045001 (2012).
[14]S. Boldyrev and J. C. Perez, "Spectrum of kinetic-Alfven turbulence," Astrophys. J. Lett. **758**, L44 (2012).
[15]L. Rudakov, M. Mithaiwala, G. Ganguli, and C. Crabtree, Phys. Plasmas **18**, 012307 (2011).
[16]L. Rudakov, C. Crabtree, G. Ganguli, and M. Mithaiwala, Phys. Plasmas **19**, 042704 (2012).
[17]R. Numata, G. G. Howes, T. Tatsuno, M. Barnes, and W. Dorland, J. Comput. Phys. **229**(24), 9347 (2010).
[18]M. Wan, W. Matthaeus, H. Karimabadi, V. Roytershteyn, M. A. Shay, P. Wu, W. Daughton, B. Loring, and S. C. Chapman, Phys. Rev. Lett. **109**, 195001 (2012).
[19]K. J. Bowers, B. J. Albright, L. Yin, B. Bergen, and T. J. T. Kwan, Phys. Plasmas **15**, 7 (2008).
[20]T. A. Yousef, T. Heinemann, A. A. Schekochihin, N. Kleeorin, I. Rogachevskii, A. B. Iskakov, S. C. Cowley, and J. C. McWilliams, Phys. Rev. Lett. **100**, 184501 (2008).
[21]K. Julien and E. Knobloch, Philos. Trans. R. Soc. London **368**, 1607 (2010).
[22]F. Sahraoui, M. L. Goldstein, P. Robert, and Y. V. Khotyaintsev, Phys. Rev. Lett. **102**, 231102 (2009).
[23]O. Alexandrova, V. Carbone, P. Veltri, and L. Sorriso-Valvo, Astrophys. J. **674**, 1153 (2008).
[24]B. A. Maruca, J. C. Kasper, and S. D. Bale, Phys. Rev. Lett. **107**, 201101 (2011).
[25]N. P. Korzhov, V. V. Mishin, and V. M. Tomozov, Planet. Space Sci. **32**, 1169 (1984).
[26]D. A. Roberts, M. L. Goldstein, W. H. Matthaeus, and S. Ghosh, J. Geophys. Res., [Space Phys.] **97**, 17115, doi:10.1029/92JA01144 (1992).
[27]G. P. Zank, W. H. Matthaeus, and C. W. Smith, J. Geophys. Res., [Space Phys.] **101**, 17093, doi:10.1029/96JA01275 (1996).
[28]B. Breech, W. H. Matthaeus, J. Minnie, J. W. Bieber, S. Oughton, C. W. Smith, and P. A. Isenberg, J. Geophys. Res., [Space Phys.] **113**, A08105, doi:10.1029/2007JA012711 (2008).
[29]J. E. Borovsky, J. Geophys. Res. **117**, A06224, doi:10.1029/2012JA017623 (2012).
[30]M. J. Lighthill, Proc. R. Soc. London **211**, 564 (1952).
[31]A. Miura and P. L. Pritchett, J. Geophys. Res., [Space Phys.] **87**, 7431, doi: 10.1029/JA087iA09p07431 (1982).
[32]K. Nykyri and A. Otto, Geophys. Res. Lett. **28**, 3565, doi:10.1029/2001GL013239 (2001).
[33]T. K. M. Nakamura, M. Fujimoto, and A. Otto, J. Geophys. Res., [Space Phys.] **113**, A09204, doi:10.1029/2007JA012803 (2008).
[34]M. Faganello, F. Califano, and F. Pegoraro, Phys. Rev. Lett. **101**, 105001 (2008).
[35]P. Dmitruk, W. Matthaeus, and N. Seenu, Astrophys. J. **617**, 667 (2004).
[36]A. Monin and A. Yaglom, *Statistical Fluid Mechanics, CTR Monograph* (MIT, 1971 and 1975), Vol. 1 and 2, no. v. 1, pt. 2.
[37]S. Bourouaine, O. Alexandrova, E. Marsch, and M. Maksimovic, Astrophys. J. **749**, 102 (2012).
[38]F. Anselmet, Y. Gagne, E. J. Hopfinger, and R. A. Antonia, J. Fluid Mech. **140**, 63 (1984).
[39]A. N. Kolmogorov, J. Fluid Mech. **13**, 82 (1962).
[40]A. M. Obukhov, J. Geophys. Res. **67**, 3011, doi:10.1029/JZ067i008p03011 (1962).
[41]K. R. Sreenivasan and R. A. Antonia, Annu. Rev. Fluid Mech. **29**, 435 (1997).

[42]S. Servidio, M. Wan, W. Matthaeus, and V. Carbone, Phys. Fluids **22**, 125107 (2010).
[43]B. Cabral and L. Leedom, in Proceedings of the 20th Annual Conference on Computer Graphics and Interactive Techniques, ACM New York, NY, 1993, pp. 263–270.
[44]J. Egedal, W. Daughton, and A. Le, Nat. Phys. **8**, 321 (2012).
[45]E. Marsch, Living Rev. Solar Phys. **3**, 1 (2006).
[46]B. J. Vasquez, C. W. Smith, K. Hamilton, B. T. MacBride, and R. J. Leamon, J. Geophys. Res. **112**, A07101, doi:10.1029/2007JA012305 (2007).
[47]K. T. Osman, W. H. Matthaeus, A. Greco, and S. Servidio, Astrophys. J. Lett. **727**, L11 (2011).
[48]V. Roytershteyn, W. Daughton, H. Karimabadi, and F. S. Mozer, Phys. Rev. Lett. **108**, 185001 (2012).
[49]D. Sundkvist, A. Retino, A. Vaivads, and S. D. Bale, Phys. Rev. Lett. **99**, 025004 (2007).
[50]A. A. Schekochihin, S. C. Cowley, W. Dorland, G. W. Hammett, G. G. Howes, E. Quataert, and T. Tatsuno, Astrophys. J. **182**, 310 (2009).